

High throughput hemogram of T cells using digital holographic microscopy and deep learning

Roopam K. Gupta^{a,*}, Nils Hempler^c, Graeme P. A. Malcolm^e, Kishan Dholakia^{c,d},
Simon J. Powis^b

^a*Atonarp Micro-Systems India Pvt. Ltd., The Millenia, Tower A, 3rd Floor, No. 1 & 2 Murphy Road, Ulsoor, Bangalore 560008 India*

^b*School of Medicine and Biomedical Sciences Research Complex, University of St. Andrews, KY16 9TF, UK*

^c*SUPA, School of Physics and Astronomy, University of St. Andrews, KY16 9SS, UK*

^d*Department of Physics, College of Science, Yonsei University, Seoul 03722, South Korea.*

^e*M Squared Lasers, 1 Kelvin Campus, West of Scotland Science Park, Glasgow, G20 0SP, UK*

Abstract

T cells of the adaptive immune system provide effective protection to the human body against numerous pathogenic challenges. Current labelling methods of detecting these cells, such as flow cytometry or magnetic bead labelling, are time consuming and expensive. To overcome these limitations, the label-free method of digital holographic microscopy (DHM) combined with deep learning has recently been introduced which is both time and cost effective. In this study, we demonstrate the application of digital holographic microscopy with deep learning to classify the key CD4⁺ and CD8⁺ T cell subsets. We show that combining DHM of varying fields of view, with deep learning, can potentially achieve a classification throughput rate of 78,000 cells per second with an accuracy of 76.2% for these morphologically similar cells. This throughput rate is 100 times faster than the previous studies and proves to be an effective replacement for labelling methods.

Keywords: Deep learning; Microscopy; Immunology; Multivariate analysis

1. Introduction

2 The adaptive immune response comprises white blood cells including T and B cells
3 that can recognise and respond in an antigen-specific manner to a vast array of potential
4 human pathogens. Of great significance, residing within this same subset of cells is the
5 ability to generate memory cells, which can produce faster and stronger secondary
6 responses. Vaccination/immunisation relies almost exclusively on the generation of
7 such memory T and B cells to protect both individuals and populations [1].

*Corresponding author; This work was performed at University of St. Andrews
Email address: roopamgupta211@gmail.com (Roopam K. Gupta)

8 T cells at the most basic level of functionality are divided into two groups based
9 upon their expression of CD4 and CD8 cell surface proteins [2]. Typically, CD4⁺ T
10 cells coordinate both B cell antibody responses and other T cells by the secretion of
11 various cytokines [3], coordinated through expression of HLA class II, whereas CD8⁺
12 T cells are usually directly capable of elimination of virally infected or tumourigenic
13 cells by the detection of specific viral or tumour antigenic peptides presented on HLA
14 class I molecules [4]. The numbers of T cells can vary significantly during the course
15 of diseases. For example, in HIV the numbers of CD4⁺ T cells can reduce to very low
16 levels over time [5], and recent data for patients with COVID-19 has shown loss of
17 both CD4⁺ and CD8⁺ population in many patients undergoing ICU-level care [6, 7, 8].

18 The identification of these cells requires destructive fixation or chemical staining
19 which is both time consuming and costly. To circumvent these issues, label-free optical
20 methods of Raman spectroscopy [9], autofluorescence lifetime imaging [10] or digital
21 holographic microscopy (DHM) have been employed [11]. These methods provide
22 molecular or morphological data and require an additional step of statistical analysis.
23 Methods such as support vector machines (SVMs), random forests (RFs) or artificial
24 neural networks (ANNs) have been popularly employed for these purposes. However,
25 due to the inherent linearity, the methods of SVM and RF have proven to be less ef-
26 ficient for classification than deep learning based ANNs [12]. Hence deep learning is
27 being ever more widely applied to solve the classification problem in biophotonics [13].

28 Another aspect of the mentioned systems is their throughput rate. While Raman
29 spectroscopy provides high molecular specificity, it is slow and lacks the aspect of
30 throughput [14]. DHM when combined with convolutional neural networks, on the
31 other hand, provides the capability to differentiate morphologically similar cells with
32 a recent demonstration of throughput rate of more than 100 cells/s [15]. This through-
33 put rate is still too low: the gold standard flow cytometry may allow a throughput rate
34 of 70,000 cells/s [16]. The throughput rate of the DHM system can be enhanced by
35 reducing the magnification and numerical aperture (NA) of the microscopic objective
36 which may in-turn result in a lower resolution of images. These lower resolution im-
37 ages system can be transformed into ones of higher resolution using the single image
38 super resolution (SISR) method of deep learning [17]. Recently, deep learning has
39 been widely applied more broadly in photonics to improve the resolution of bright field
40 optical microscope [18], to enable cross-modality super resolution in fluorescence mi-
41 croscopy [19], to facilitate pixel super-resolution in coherent imaging systems Liu et al.
42 [20], and to enhance the resolution of scanning electron microscopy [21].

43 Here, we address the use of DHM for rapid, high throughput classification of CD4⁺
44 and CD8⁺ T cells. We present a method based upon particle swarm optimization
45 (PSO) [22] to identify an optimal CNN geometry for a given dataset. Subsequently,
46 we compare the classification performance of DHM-CNN combination for different
47 optical magnifications. We also present a new method of SISR in microscopy based on
48 cycle generative adversarial networks (GANs) for the enhancement in the resolution of
49 images acquired from 20X optical magnification to images acquired from 100X optical
50 magnification. Compared to previous studies [19, 20, 21], which require an additional
51 step of co-registering the field of view (FOV), our semi-supervised method improves
52 the resolution of unpaired phase images which were independent of FOV and do not
53 require any additional analytical methods. Our approach demonstrates a possibility of

54 high throughput of 78,000 cells/s using a combination of DHM with CNNs, which is
55 nearly two orders of magnitude in excess of previous reports [15]. Importantly, this
56 result for the first time makes a label-free DHM approach comparable to the gold stan-
57 dard of flow cytometry.

58 2. Methods

59 2.1. Cell Isolation

60 This work was undertaken after ethical review from the School of Medicine at the
61 University of St. Andrews, utilising buffy coats of six different healthy donors ob-
62 tained from NHS UK. PBMC were isolated from the buffy coats by centrifugation at
63 room temperature on Ficoll-Pacque at density 1.077 g/ml (Thermofisher, UK). CD4⁺
64 and CD8⁺ T cell populations were isolated using a negative depletion method follow-
65 ing the manufacturers instructions (Dynabeads CD4⁺ T cells, 11346D and Dynabeads
66 CD8⁺ T cells, 11348D, Thermofisher UK). Following the isolation, the purified cells
67 were cultured in RPMI 1640 supplemented with 5 % Foetal Bovine Serum (both Ther-
68 mofisher, UK).

69 Flow cytometry was employed to confirm the purity of the purified cell samples.
70 Each cell type was stained with combinations of antibodies CD3-PE and -FITC, clone
71 HIT3a, eBioscience UK, CD4-PE and -FITC, clone OKT4, eBioscience UK, CD8-
72 PE and -AF488, clones SK1, eBioscience UK, and FAB1509G, R&D UK. Cells were
73 analysed on a Guava 8HT cytometer (Merck Millipore, UK).

74 For the optical analysis, the cells were resuspended in Phosphate Buffer Saline
75 (PBS) with 0.5% FBS solution to avoid aggregation. 20 μ l of cell suspension was
76 transferred to the center of a clean quartz slide (25.4 mm \times 25.4 mm \times 1 mm) chamber
77 - formed by a 100 μ m thick vinyl spacer. This chamber was covered from the top using
78 a thin quartz slide (25.4 mm \times 25.4 mm, 0.11 mm - 0.15 mm thickness) and finally the
79 whole assembly was inverted and left for ~20 minutes to avoid cellular motion.

80 2.2. Digital holographic microscopy

81 We modified a previously employed off-axis digital holographic microscope to cap-
82 ture the holographic images of the cells with three different optical configurations [15].
83 As shown in Fig. 1, the optical configurations were varied by changing the microscopic
84 objectives to ones with magnifications of 20X (NA = 0.4, Nikon Japan 130314), 60X
85 (NA = 0.8, Nikon) and 100X (NA = 0.9, Nikon Japan 230538) respectively. The sam-
86 ple was placed between the two objectives and the image was interfered with the light
87 from the reference arm at the surface of the CCD camera (Ximea XiQ MQ013MG-E2).
88 This camera was set to accumulate 16 bit images with a frame rate of 60 fps and an
89 exposure time of 33.3 ms.

90 We acquired the data for the two cell types separately for each optical configuration.
91 The data acquired using the three objectives varied with the magnification. With an
92 increase in magnification, the field of view (FOV) was reduced. For the 20X objective
93 (lateral resolution: 0.66 μ m; axial resolution: 6.65 μ m), we achieved an FOV of 100
94 μ m \times 130 μ m; for the 60X objective (lateral resolution: 0.31 μ m; axial resolution: 1.47
95 μ m), we achieved 68 μ m \times 64 μ m for the FOV and 100X objective (lateral resolution:

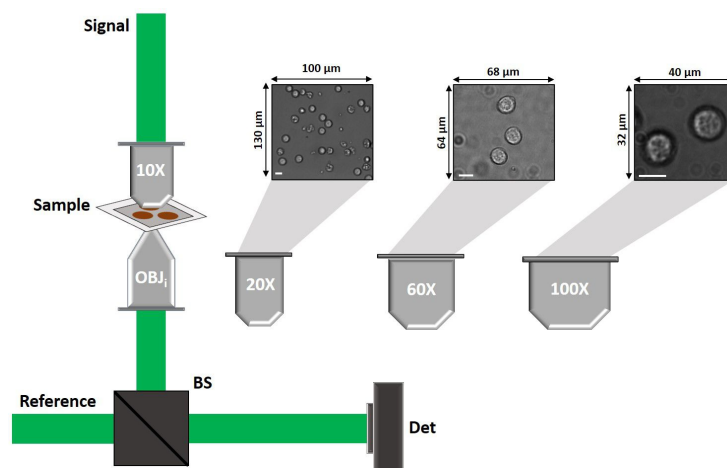


Figure 1: **Schematic of different optical configurations used with digital holographic microscope.** The three objectives with the magnifications of 20X, 60X and 100X were employed for data acquisition. The sub figures indicate three bright field FOVs acquired for each objective. The scale bar indicates $10 \mu\text{m}$ for each image.

96 $0.29 \mu\text{m}$; axial resolution: $1.31 \mu\text{m}$) allowed for an FOV of $40 \mu\text{m} \times 32 \mu\text{m}$. Since
97 these FOVs provide with cell images of different radii (in px), we implemented Haugh
98 transform based method.

99 2.3. *k-means segmentation*

100 The phase images calculated using the three optical configurations demonstrate dif-
101 ferent degrees of resolutions. Hence to identify and understand the degree of granu-
102 larity discovered using each configuration, we implemented a method of k-means cluster-
103 ing based image segmentation [23]. We considered the phase images corresponding to
104 each configuration individually. To identify the number of segmentation classes across
105 the cellular structure, we increased the number of segmentation classes in steps of unity
106 until the algorithm returned a solution with discontinuous boundaries.

107 In this specific case of DHM, as the phase images represent the refractive index
108 variation across the image, the classes represent this distribution. This in turn demon-
109 strates the variation of granularity analyzed using the phase images evaluated using
110 each FOV.

111 2.4. *Optimization of the CNN geometry*

112 The phase images obtained using the three configurations were of different sizes,
113 for the 20X objective the phase images were 52×52 pixels (px) whereas for the 60X
114 objective, the phase images were of size 100×100 px and for 100X objective the phase
115 images were acquired with a size of 200×200 px. We optimized a CNN geometry for
116 each of the three configuration by implementing a PSO based approach. PSO is a type
117 of swarm intelligence method for global optimization where each individual (called
118 particle) of the population (called swarm) adjust their trajectory towards the previous

119 best position attained by any member of their topological neighborhood. This approach
 120 is used to minimize the error output of an objective function. In our case, we consider
 121 the objective function as the classification sensitivity and specificity achieved using a
 122 given network geometry (particle).

123 To identify the best CNN geometries, we divided the complete dataset for each op-
 124 tical configuration into training, validation and test sets such that the training/validation
 125 set and testing set came from different donors. Details of segmentation of above
 126 datasets have been summarised in table 1.

S.No.	20X		60X		100X	
	CD4	CD8	CD4	CD8	CD4	CD8
Train/Val	2385	2056	1066	971	704	704
Test	344	323	84	77	104	96

Table 1: Table summarizing the total number of single cells phase images considered for different optical configurations.

127 We implemented the PSO algorithm by constructing an objective function in the
 128 form of a training instance. Each training instance was designed to develop a network
 129 geometry and providing the performance of the geometry on the validation dataset.
 130 For each training instance, we trained the CNNs using an Adam optimizer [24] with
 131 maximum epochs set at 100, initial learning at 1×10^{-3} , L2 regularization at 5×10^{-6} ,
 132 validation frequency at 40 iterations and validation patience of 5 iterations with a mini
 133 batch size of 128 images. The network geometry was developed by the virtue of pa-
 134 rameters in the form of each particle in the PSO algorithm. These parameters dictated
 135 the number of layers, type of layers, number of filters in each layer, stride and padding
 136 for each layer. To conserve maximal input image information, the convolution layers
 137 were restricted with filter sizes between 1 and 5. To conserve the memory of system
 138 and avoid over estimation, number of convolution filters for any layer were restricted
 139 to a maximum of 50. The number of neurons in fully connected layer and the dropout
 140 ratio were restricted to be more than zero. To conserve the network geometry, the input
 141 layer was set as image input layer with the size of image in the dataset and the output
 142 layer was set with fully connected layer with 2 neurons (representing each class) fol-
 143 lowed by softmax layer and a classification layer. We evaluated the cost function for
 144 each training instance as:

$$\text{Sensitivity} = \frac{TP}{TP + FN} \quad (1a)$$

$$\text{Specificity} = \frac{TN}{TN + FP} \quad (1b)$$

$$\text{Cost} = 1 - \frac{\text{Sensitivity} + \text{Specificity}}{2} \quad (1c)$$

145 Here, in Eq. 1a and 1b, TP is true positive, TN is true negative, FP is false positive and
 146 FN is false negative.

147 We considered a total of 40 particles and a single swarm (optimized from 2 to 60
 148 in the steps of one unit to avoid divergence) to find isolate an optimal architecture

149 of CNN for each image size. Each particle's position and velocity were initialized
 150 randomly. After the calculation of cost for all the particles, the particle with least cost
 151 was considered as the reference such that the position and velocity of all the other
 152 particles were updated relatively to the reference.

153 2.5. Cycle generative adversarial training for image transformation

154 The phase images evaluated using the three optical configuration show variability
 155 in the resolution due to different resolving powers of the microscopic objectives. As
 156 mentioned in section 2.2, the phase images evaluated from the 20X objective show
 157 the least resolution whereas the images captured using 100X objective display high-
 158 est resolution. Hence to gather high resolution images with high throughput rate, we
 159 considered training a CNN to transform the images acquired using 20X objective into
 160 images acquired using 100X objective. In the current DHM system, it is very challeng-
 161 ing to identify same cells using two different configurations, hence we trained the deep
 162 networks on unpaired images using cycle-generative adversarial training [25, 26].

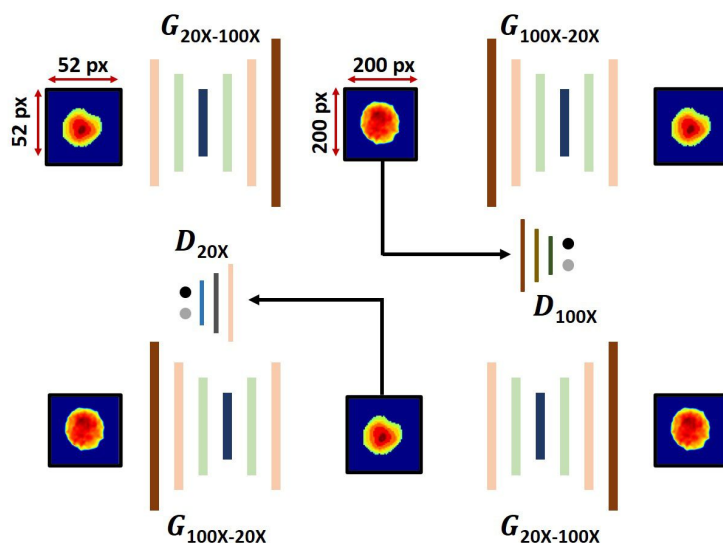


Figure 2: **Schematic of cycle GAN model applied for super-resolving the phase images.** The generative models $\mathcal{G}_{20X \rightarrow 100X}$ and $\mathcal{G}_{100X \rightarrow 20X}$ are trained with in a cycle consistent manner such that the inverse transformation of the images is conserved.

163 As shown in Fig. 2, we developed two CNNs such that the input image could be
 164 down-sampled and then up-sampled to a required size at the output. For the trans-
 165 formation of phase images captured using 20X optical configuration to 100X optical con-
 166 figuration, we developed and optimized a 54 layered CNN ($\mathcal{G}_{20X \rightarrow 100X} := \mathcal{G}_a$) whereas
 167 for the inverse translation, we developed a 34 layered CNN ($\mathcal{G}_{100X \rightarrow 20X} := \mathcal{G}_b$). These
 168 networks were optimized by changing the network filters in the step of 8 units with
 169 respect to their performance on validation dataset. With respect to the training mod-
 170 ule requirement, we also developed and two discriminator networks with 23 layers

171 ($\mathcal{D}_{100X} := \mathcal{D}_a$) and 15 layers ($\mathcal{D}_{20X} := \mathcal{D}_b$) respectively. We trained these networks
 172 with 300 randomly selected phase images each of CD4⁺ and CD8⁺ T cells from both
 173 the 20X and 100X optical configurations. Out of these, we considered 225 images for
 174 training and 75 images for validation.

175 For each training instance, we calculated a generative adversarial loss for both the
 176 generative networks. We also calculated a cycle consistency loss using the combination
 177 of two networks. The generative adversarial loss was evaluated as:

$$\mathcal{L}_{\text{GAN}}(\mathcal{G}_i, \mathcal{D}_i, X, Y) = \mathbf{E}_{y \sim p_{\text{data}}(y)}[\log \mathcal{D}_i(y)] + \mathbf{E}_{x \sim p_{\text{data}}(x)}[\log(1 - \mathcal{D}_i(\mathcal{G}_a(x)))] \quad (2)$$

178 Here, $i \in \{a, b\}$. The cycle consistency loss $\mathcal{L}_{\text{cyc}}(\mathcal{G}_a, \mathcal{G}_b)$ is computed, to satisfy the
 179 condition $x \rightarrow \mathcal{G}_a(x) \rightarrow \mathcal{G}_b(\mathcal{G}_a(x)) \approx x$, as:

$$\mathcal{L}_{\text{cyc}}(\mathcal{G}_a, \mathcal{G}_b) = \mathbf{E}_{x \sim p_{\text{data}}(x)}[\|\mathcal{G}_b(\mathcal{G}_a(x)) - x\|_1] + \mathbf{E}_{y \sim p_{\text{data}}(y)}[\|\mathcal{G}_a(\mathcal{G}_b(y)) - y\|_1] \quad (3)$$

180 Here, the variables x and y represent the input and output images for the given network
 181 configuration. The combined loss was calculated as:

$$\begin{aligned} \mathcal{L}(\mathcal{G}_a, \mathcal{G}_b, \mathcal{D}_a, \mathcal{D}_b) &= \mathcal{L}_{\text{GAN}}(\mathcal{G}_a, \mathcal{D}_a, X, Y) \\ &+ \mathcal{L}_{\text{GAN}}(\mathcal{G}_b, \mathcal{D}_b, Y, X) \\ &+ \lambda \mathcal{L}_{\text{cyc}}(\mathcal{G}_a, \mathcal{G}_b) \end{aligned} \quad (4)$$

182 Here, λ is a hyperparameter which we chose as 10 for this application. During the
 183 training, the objective is to minimize the combined loss for the generator networks
 184 while maximizing the loss for the discriminator networks:

$$\mathcal{G}_a^*, \mathcal{G}_b^* = \arg \min_{\mathcal{G}_a, \mathcal{G}_b} \max_{\mathcal{D}_a, \mathcal{D}_b} \mathcal{L}(\mathcal{G}_a, \mathcal{G}_b, \mathcal{D}_a, \mathcal{D}_b) \quad (5)$$

185 To achieve minimum training loss and avoid divergence during training, we consid-
 186 ered the training batch images in the mini-batches of 45 images. An Adam optimizer
 187 was considered with a learning rate of 2×10^{-4} , gradient descent factor of 0.5 and a
 188 squared gradient descent factor of 0.99. We validated the network performance after 25
 189 iterations using 25 randomly sampled images for both the cell types from the validation
 190 set. The training was continued for a total of 5000 epochs.

191 3. Results

192 3.1. Cell isolation

193 Untouched human blood CD4⁺ and CD8⁺ T cells were obtained by negative de-
 194pletion, in which other cells not of interest were removed using cell-lineage specific
 195antibodies. Flow cytometry (Fig. 3) confirmed the purity of the cell populations in line
 196with our previous studies [27, 28] with CD4⁺ cells isolated at an average of 89% (n=3)
 197and CD8⁺ cells at an average of 86% (n=3).

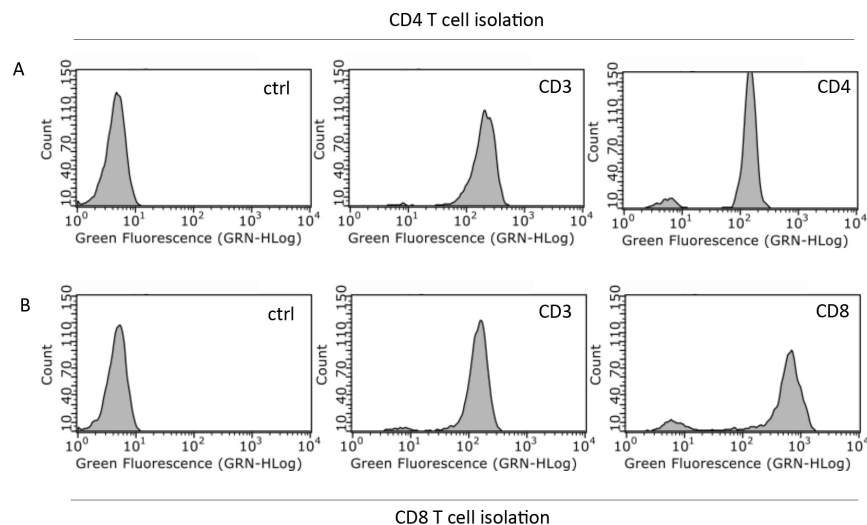


Figure 3: **Representative flow cytometric plots of CD4 and CD8 T cells purified by negative depletion.** Purified cell samples were stained with anti-CD3, -CD4 or -CD8-FITC or AF488 coupled antibodies and analysed by flow cytometry for (A) CD4 T cells and (B) CD8 T cells. Average purity of three separate purifications is reported in the main text.

198 3.2. Automated detection of cells and phase image calculation

199 We captured bright field and fringe images using all the three configurations de-
200 scribed above. These images presented with variable radii of single cells, hence to
201 automatically detect these cells, we implemented Haugh transform using a prewritten
202 MATLAB script [29].

203 We optimized the search parameters of radii, gradient threshold and radius of search
204 filter with respect to the images acquired for each configuration. In order to opti-
205 mize these parameters, we considered the size of cells, mean magnitude of gradient for
206 empty space and the radius of cells for each configuration.

207 The images accumulated using the three optical configuration exhibit varying FOVs
208 and resolutions. Fig. 4 demonstrate the automatic cellular detection for various FOVs.
209 As summarised in Table 2, the FOV achieved by using the 20X objective was greatest at
210 $100\ \mu\text{m} \times 130\ \mu\text{m}$ (which may allow imaging a maximum of 1300 cells in one snapshot
211 which potentially allowed a throughput rate of 78,000 cells per second), however, the
212 resolution of the accumulated images was poor. For imaging using the 60X objective,
213 a smaller FOV of $68\ \mu\text{m} \times 64\ \mu\text{m}$ was achieved (allowing a maximum of 36 cells
214 resulting in the highest possible throughput of 2,160 cells per second) with a reasonable
215 resolution. Imaging using the 100X objective resulted in a much smaller FOV of $40\ \mu\text{m}$
216 $\times 32\ \mu\text{m}$ (enclosing a maximum of 12 cells and allowing a highest possible throughput
217 of 720 cells per second) with the highest resolution.

218 With respect to the numerical aperture of the microscopic objectives, the retrieved
219 phase images show the differences in resolution. The phase image recovered using 20X

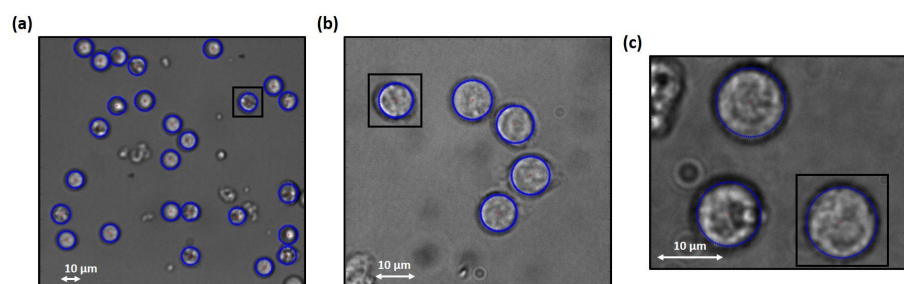


Figure 4: **Automatic detection of cells using Haugh transform** Subsection of Bright field images recovered from (a) 20X Objective ($100 \mu\text{m} \times 130 \mu\text{m}$) (b) 60X objective ($68 \mu\text{m} \times 64 \mu\text{m}$) and (c) 100X objective ($40 \mu\text{m} \times 32 \mu\text{m}$). Blue highlighted regions represent the automatic detection of cells for three FOV's using Haugh transform circular detection. Here the boxes show the cropped area of images for single cells.

Optical Configuration	Field of View	Realizable Throughput
20X	$100 \times 130 \mu\text{m}$	78000 cells/s
60X	$68 \times 64 \mu\text{m}$	2160 cells/s
100X	$40 \times 32 \mu\text{m}$	720 cells/s

Table 2: Summary of field of views and maximum realizable throughput for the three optical configurations.

220 objective with a numerical aperture (NA) of 0.4, displays the least resolution (lateral:
 221 $0.66 \mu\text{m}$; axial: $6.65 \mu\text{m}$) for both the cell lines (Fig. 5 (a),(d)). The application of
 222 60X objective with the NA of 0.8 results in moderately resolved (lateral resolution:
 223 $0.31 \mu\text{m}$; axial resolution: $1.47 \mu\text{m}$) phase images (Fig. 5 (b),(e)) and the phase images
 224 calculated from the fringe images captured using the 100X objective (with the NA of
 225 0.9) were highly resolved (lateral resolution: $0.29 \mu\text{m}$; axial resolution: $1.31 \mu\text{m}$).

226 After the extraction of single cell phase images, we employed k-means clustering
 227 based segmentation to quantify the granularity achieved using different configurations.
 228 As anticipated, the phase images of the two cell types show a very similar variation
 229 in resolution with respect to the objectives. As shown in sub-figures of Fig. 5, the
 230 algorithm when applied over the phase images of the two cells for the 20X objective,
 231 saturated at 8 segments. For the phase images accumulated using 60X objective, the
 232 algorithm saturated at 9 segments for CD4 cells whereas it saturated at 10 segments for
 233 the CD8 cells. For its application on phase images evaluated using 100X objective, the
 234 algorithm presented a saturation at 11 segments for both the cell types.

235 These results clearly demonstrate that the images acquired using the three objec-
 236 tives show a variability in resolution. It is also evident that with an increase in the
 237 numerical aperture of the objective, these images provide the information of a wider
 238 range of variations across the cellular structure.

239 3.3. Classification of phase images

240 The next step for the analysis of the single phase images was to classify them
 241 with respect to the cell types. This was achieved by employing the CNNs which were

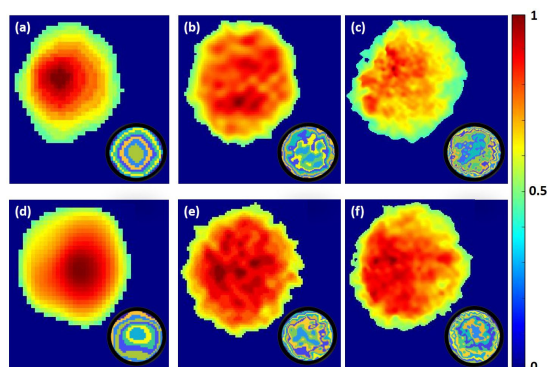


Figure 5: **Normalized phase images of T Cells.** Single cell normalized phase images of the CD4 cells retrieved using (a) 20X objective (b) 60X objective (c) 100 X objective; Single cell normalized phase images of CD8 cells retrieved using (d) 20X objective (e) 60X objective (f) 100X objective. Colorbar represents the normalized phase gain of the signal arm with respect to the reference arm. Here the sub figures are the k-means based image segmentation of these images.

242 optimized by implementing PSO algorithm as explained before.

243 The three optical configurations, resulted in different sizes of single cell phase im-
244 ages as 52×52 px for 20 X objective, 100×100 px for 60 X objective and 200×200
245 px for 100X objective. Hence the optimal CNN geometry also displayed a variation in
246 size. For the 20X optical configuration, the optimal CNN geometry was identified with
247 a total of six layers with 39,998 parameters. Using the validation set, the CNN returned
248 a sensitivity of $63.13 \% \pm 2.23 \%$ and specificity of $64.93\% \pm 5.65\%$, whereas when
249 considered for the test dataset, the CNN resulted in a sensitivity of $64.07 \% \pm 2.64 \%$
250 and a specificity of $56.83 \% \pm 2.36 \%$.

251 For the 60X optical configuration, the optimal CNN geometry was identified as a
252 slightly longer network. This geometry comprised a total of 16 layers with 226,707
253 parameters. On the validation set, the classification efficiency of the CNN resulted in
254 $70.94 \% \pm 2.27 \%$ sensitivity and $65.52 \% \pm 2.08\%$ specificity, whereas on the test
255 set the trained CNN resulted in a specificity of $69.92 \% \pm 3.91\%$ and a sensitivity of
256 $69.59 \% \pm 3.10 \%$. Finally, the optimization routine was also implemented on the
257 phase images acquired using the 100X optical configuration and this resulted in a CNN
258 geometry of 24 layers with 1,603,327 parameters. This geometry when applied over
259 the phase images from validation dataset resulted in the specificity of $80.28 \% \pm 1.17$
260 $\%$ and a sensitivity of $77.77 \% \pm 2.72 \%$. The specificity and sensitivity calculated
261 using the test data were $82.5 \% \pm 3.96 \%$ and $73.18 \% \pm 7.55 \%$ respectively.

262 The interesting aspect of this comparison is the trend of increasing classification
263 accuracy (Fig. 6) and decreasing throughput rate with respect to the optical configu-
264 ration. For the 20X configuration, the optimal CNN geometry resulted in a validation
265 accuracy of $62.28 \% \pm 2.54 \%$ and $59.43 \% \pm 1.99 \%$ as the test accuracy with an
266 allowed maximum throughput rate of 78,000 cells per second. For the optical configu-
267 ration with 60X magnification microscopic objective, the optimum CNN resulted in

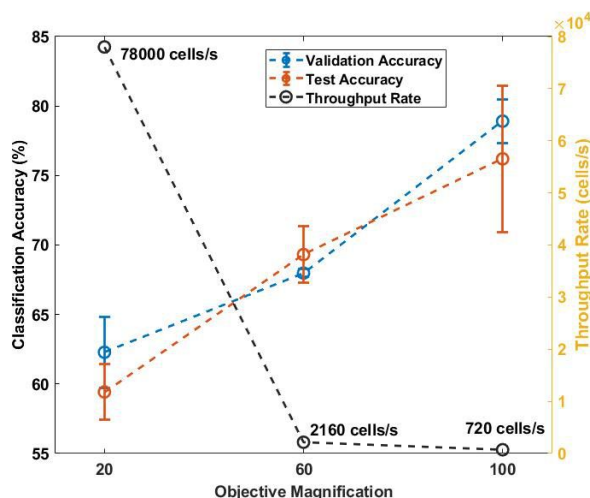


Figure 6: **Comparison between throughput rate and classification accuracy obtained using different optical configurations.** For the validation set, the values for classification accuracy range from 62.28 % \pm 2.54 % for 20X objective, 69.31 % \pm 2.04 % for 60X objective and 78.91 % \pm 1.57 % for 100X objective. For the test set, a classification accuracy of 59.43 % \pm 1.99 % for 20X objective, 69.31 % \pm 2.04 % for 60X objective and 76.2 % \pm 5.27 % for 100X objective was obtained. The three optical configurations allow for 78000 cells/s, 2160 cells/s and 720 cells/s as the throughput rate for 20X, 60X and 100X objective respectively. Here the curve in blue represents classification accuracy for validation set, curve in red represents the accuracy for test set and curve in black shows the variation in throughput rate for the three configurations.

268 67.98 % \pm 0.27 % validation accuracy and 69.31 % \pm 2.04 % test accuracy. While
269 considering the dataset accumulated using the microscopic objective with 100X mag-
270 nification, the optimal CNN geometry resulted in a maximum classification accuracy
271 with 78.91 % \pm 1.57 % for validation set and 76.2 % \pm 5.27 % for the test set. These
272 results confirm that by increasing the magnification of a holographic system, one may
273 acquire an increasingly more precise classification of immune cells. However, with in-
274 creasing magnification the throughput limit of the system deteriorates. Hence to keep
275 an increased throughput limit and simultaneously improving the classification ability
276 of the system, we trained another deep learning based model to transform the phase
277 images acquired from 20X configuration to the phase images which may represent the
278 acquisition from 100X optical configuration.

279 3.4. Image transformation and classification

280 The single image super resolution transformation was implemented on the phase
281 images acquired using 20X configuration to convert them into the phase images ac-
282 quired using 100X configuration. To achieve this the DL models were trained using
283 the cycle GAN training method as explained before.

284 The trained generative models resulted in astounding transformations of the phase
285 images. As shown in Fig. 7, the trained deep generative model transformed the phase
286 images with a high speed of 6.89 milliseconds per transformation (limited by the the
287 processing power of the computer which can further be improved). In the mentioned

288 figure, (a) shows the transformation of $CD4^+$ T cells from 20X configuration into 100X
289 configuration; (b) demonstrates the same transformation of $CD8^+$ T cells. An interest-
290 ing aspect which is visible on the transformed images is that the deep models auto-
291 matically learned to draw an outline around the periphery of the cells. Another aspect
292 which is evidently visible from these transformations is the variation in the shape of the
293 cells. This can be explained with respect to the cycle GAN type training module. The
294 CNNs trained with this training module learn to transform and simultaneously inverse
295 transform the images between the two domains. This learning process makes sure that
296 the statistics and the functional relationship between the two domains are maintained.

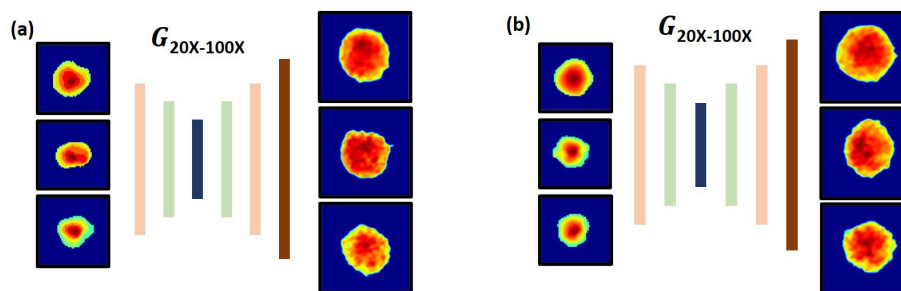


Figure 7: **Demonstration of image transformation using the trained deep generative model.** Transformation of phase images of (a) $CD4^+$ and (b) $CD8^+$ T cells acquired from 20X optical configuration into 100X optical configuration.

297 After the transformation of the phase images, we performed a classification using
298 the pre-trained optimal CNN geometry. This resulted in the classification accuracy of
299 $45.93 \% \pm 2.46 \%$ for the validation set and $47.91 \% \pm 2.05 \%$ for the test set. These
300 values were below the expectation and which may be explained due to the presence of
301 boundaries and overall shape orientation of the cells. Hence, to overcome these prob-
302 lems, we re-trained the previously trained networks on the transformed image dataset.
303 This resulted in satisfactory results with sensitivity of $81.55 \% \pm 0.81 \%$ and a speci-
304 ficity of $84.72 \% \pm 1.16 \%$ for the validation set and, the sensitivity and specificity of
305 $79.77 \% \pm 3.32 \%$ and $81.77 \% \pm 1.51 \%$ for test set respectively.

306 These results display the increased capability in terms of classification accuracy for
307 the 20X optical configuration. Hence, the application of cycle generative models would
308 be beneficial for improving the resolution of system and simultaneously improving the
309 throughput rate by up to two orders of magnitude.

310 4. Conclusion

311 In conclusion, we have presented a comparative study for the label free classifica-
312 tion of T-cell subsets namely $CD4^+$ and $CD8^+$ T cells using a combination of digital
313 holographic microscopy and convolutional neural networks. We compare the perfor-
314 mance of DHM - CNN based classification by considering three different optical con-
315 figurations. These configurations were considered by changing the optical magnifica-
316 tion of the microscopic objectives between 20X, 60X and 100X. The T - cell subsets,

317 being morphologically very similar, makes it very challenging for classification using
318 the CNNs. Hence we report a maximal classification accuracy of 76.2% by using a
319 microscopic objective with 100X magnification. Additionally, we demonstrate that the
320 application of cycle GAN type training may help in enhancing the throughput rate and
321 resolution of a DHM based system by up to two orders of magnitude.

322 **Author Contributions**

323 KD and SJP developed the project. RKG performed the experiments and developed
324 the numerical analysis procedures. RKG wrote the paper with contributions from SJP
325 and KD which was approved by NH and GPAM. KD, SJP and NH supervised the
326 project.

327 **References**

- 328 [1] B. Pulendran, R. Ahmed, Immunological mechanisms of vaccination, *Nature*
329 *immunology* 12 (2011) 509.
- 330 [2] W. Ellmeier, S. Sawada, D. R. Littman, The regulation of cd4 and cd8 coreceptor
331 gene expression during t cell development, *Annual review of immunology* 17
332 (1999) 523–554.
- 333 [3] K. A. Read, M. D. Powell, B. K. Sreekumar, K. J. Oestreich, In vitro differentia-
334 tion of effector cd4+ t helper cell subsets, in: *Mouse Models of Innate Immunity*,
335 Springer, 2019, pp. 75–84.
- 336 [4] A. M. Van der Leun, D. S. Thommen, T. N. Schumacher, Cd8+ t cell states in
337 human cancer: insights from single-cell analysis, *Nature Reviews Cancer* (2020)
338 1–15.
- 339 [5] G. Doitsh, W. C. Greene, Dissecting how cd4 t cells are lost during hiv infection,
340 *Cell host & microbe* 19 (2016) 280–291.
- 341 [6] N. P. Restifo, M. E. Dudley, S. A. Rosenberg, Adoptive immunotherapy for
342 cancer: harnessing the t cell response, *Nature Reviews Immunology* 12 (2012)
343 269–281.
- 344 [7] D. M. Pardoll, The blockade of immune checkpoints in cancer immunotherapy,
345 *Nature Reviews Cancer* 12 (2012) 252–264.
- 346 [8] B. Diao, C. Wang, Y. Tan, X. Chen, Y. Liu, L. Ning, L. Chen, M. Li, Y. Liu,
347 G. Wang, et al., Reduction and functional exhaustion of t cells in patients with
348 coronavirus disease 2019 (covid-19), *Frontiers in Immunology* 11 (2020) 827.
- 349 [9] M. Chen, N. McReynolds, E. C. Campbell, M. Mazilu, J. Barbosa, K. Dholakia,
350 S. J. Powis, The use of wavelength modulated raman spectroscopy in label-
351 free identification of t lymphocyte subsets, natural killer cells and dendritic cells,
352 *PLoS One* 10 (2015) e0125158.

- 353 [10] A. J. Walsh, K. P. Mueller, K. Tweed, I. Jones, C. M. Walsh, N. J. Piscopo, N. M.
354 Niemi, D. J. Pagliarini, K. Saha, M. C. Skala, Classification of t-cell activation
355 via autofluorescence lifetime imaging, *Nature Biomedical Engineering* (2020)
356 1–12.
- 357 [11] N. McReynolds, F. G. Cooke, M. Chen, S. J. Powis, K. Dholakia, Multimodal
358 discrimination of immune cells using a combination of raman spectroscopy and
359 digital holographic microscopy, *Scientific reports* 7 (2017) 43631.
- 360 [12] E. Raczek, B. Zagajewski, Comparison of support vector machine, random forest
361 and neural network classifiers for tree species classification on airborne hyper-
362 spectral apex images, *European Journal of Remote Sensing* 50 (2017) 144–154.
- 363 [13] P. Pradhan, S. Guo, O. Ryabchykov, J. Popp, T. W. Bocklitz, Deep learning a
364 boon for biophotonics?, *Journal of Biophotonics* 13 (2020) e201960186.
- 365 [14] L. Woolford, M. Chen, K. Dholakia, C. S. Herrington, Towards automated cancer
366 screening: label-free classification of fixed cell samples using wavelength modu-
367 lated raman spectroscopy, *Journal of biophotonics* 11 (2018) e201700244.
- 368 [15] R. K. Gupta, M. Chen, G. P. Malcolm, N. Hempler, K. Dholakia, S. J. Powis,
369 Label-free optical hemogram of granulocytes enhanced by artificial neural net-
370 works, *Optics express* 27 (2019) 13706–13720.
- 371 [16] J. Picot, C. L. Guerin, C. Le Van Kim, C. M. Boulanger, Flow cytometry: re-
372 spective, fundamentals and recent instrumentation, *Cytotechnology* 64 (2012)
373 109–130.
- 374 [17] W. Yang, X. Zhang, Y. Tian, W. Wang, J.-H. Xue, Q. Liao, Deep learning for
375 single image super-resolution: A brief review, *IEEE Transactions on Multimedia*
376 21 (2019) 3106–3121.
- 377 [18] Y. Rivenson, Z. Göröcs, H. Günaydin, Y. Zhang, H. Wang, A. Ozcan, Deep
378 learning microscopy, *Optica* 4 (2017) 1437–1443.
- 379 [19] H. Wang, Y. Rivenson, Y. Jin, Z. Wei, R. Gao, H. Günaydin, L. A. Bentolila,
380 C. Kural, A. Ozcan, Deep learning enables cross-modality super-resolution in
381 fluorescence microscopy, *Nature methods* 16 (2019) 103–110.
- 382 [20] T. Liu, K. De Haan, Y. Rivenson, Z. Wei, X. Zeng, Y. Zhang, A. Ozcan, Deep
383 learning-based super-resolution in coherent imaging systems, *Scientific reports* 9
384 (2019) 1–13.
- 385 [21] K. de Haan, Z. S. Ballard, Y. Rivenson, Y. Wu, A. Ozcan, Resolution enhance-
386 ment in scanning electron microscopy using deep learning, *Scientific Reports* 9
387 (2019) 1–7.
- 388 [22] J. Kennedy, R. Eberhart, Particle swarm optimization, in: *Proceedings of*
389 *ICNN'95-International Conference on Neural Networks*, volume 4, IEEE, 1995,
390 pp. 1942–1948.

- 391 [23] D. Arthur, S. Vassilvitskii, K-means++: The advantages of careful seeding,
392 in: Proceedings of the Eighteenth Annual ACM-SIAM Symposium on Discrete
393 Algorithms, SODA '07, Society for Industrial and Applied Mathematics, USA,
394 2007, p. 1027–1035.
- 395 [24] D. P. Kingma, J. Ba, Adam: A method for stochastic optimization, arXiv preprint
396 arXiv:1412.6980 (2014).
- 397 [25] J.-Y. Zhu, T. Park, P. Isola, A. A. Efros, Unpaired image-to-image translation
398 using cycle-consistent adversarial networks, in: Proceedings of the IEEE inter-
399 national conference on computer vision, 2017, pp. 2223–2232.
- 400 [26] G. Choi, D. Ryu, Y. Jo, Y. S. Kim, W. Park, H.-s. Min, Y. Park, Cycle-consistent
401 deep learning approach to coherent noise reduction in optical diffraction tomog-
402 raphy, *Optics express* 27 (2019) 4927–4943.
- 403 [27] M. Chen, N. McReynolds, E. C. Campbell, M. Mazilu, J. Barbosa, K. Dholakia,
404 S. J. Powis, The use of wavelength modulated raman spectroscopy in label-
405 free identification of t lymphocyte subsets, natural killer cells and dendritic cells,
406 *PLOS ONE* 10 (2015) 1–14.
- 407 [28] N. McReynolds, F. G. M. Cooke, M. Chen, S. J. Powis, K. Dholakia, Multimodal
408 discrimination of immune cells using a combination of raman spectroscopy and
409 digital holographic microscopy, *Scientific Reports* 7 (2017).
- 410 [29] T. Peng, Detect circles with various radii in grayscale image via hough transform,
411 Available at [https://www.mathworks.com/matlabcentral/fileexchange/9168-](https://www.mathworks.com/matlabcentral/fileexchange/9168-detect-circles-with-various-radii-in-grayscale-image-via-hough-transform)
412 [detect-circles-with-various-radii-in-grayscale-image-via-hough-transform](https://www.mathworks.com/matlabcentral/fileexchange/9168-detect-circles-with-various-radii-in-grayscale-image-via-hough-transform)
413 (2020).